
Availability-aware Sensor Fusion via Unified Canonical Space

Dong-Hee Paek Seung-Hyun Kong*
CCS Graduate School of Mobility
KAIST
{donghee.paek, skong}@kaist.ac.kr

Abstract

Sensor fusion of camera, LiDAR, and 4-dimensional (4D) Radar has brought a significant performance improvement in autonomous driving. However, there still exist fundamental challenges: deeply coupled fusion methods assume continuous sensor availability, making them vulnerable to sensor degradation and failure, whereas sensor-wise cross-attention fusion methods struggle with computational cost and unified feature representation. This paper presents availability-aware sensor fusion (ASF), a novel method that employs unified canonical projection (UCP) to enable consistency in all sensor features for fusion and cross-attention across sensors along patches (CASAP) to enhance robustness of sensor fusion against sensor degradation and failure. As a result, the proposed ASF shows a superior object detection performance to the existing state-of-the-art fusion methods under various weather and sensor degradation (or failure) conditions. Extensive experiments on the K-Radar dataset demonstrate that ASF achieves improvements of 9.7% in AP_{BEV} (87.2%) and 20.1% in AP_{3D} (73.6%) in object detection at IoU=0.5, while requiring a low computational cost. All codes are available at <https://github.com/kaist-avelab/k-radar>.

1 Introduction

Autonomous driving technology has advanced rapidly, with multiple companies adopting multi-sensor fusion approaches that combine two or more sensors, such as cameras, LiDAR, and 4-dimensional (4D) Radar, to achieve more robust and reliable perception (Badue et al., 2021; Wang et al., 2020). Cameras uniquely provide color information but struggle with depth estimation; LiDAR delivers high-resolution 3-dimensional (3D) point cloud data but is less reliable in adverse weather conditions (Zheng et al., 2023a); and 4D Radar, despite its relatively low angular resolution, offers robustness in adverse weather and directly measures relative velocity (Paek et al., 2022; Palffy et al., 2022; Kong et al., 2024; Sun and Zhang, 2021). This complementary nature initiated sensor fusion between camera, LiDAR, and 4D Radar to improve perception performance and reliability compared to a single-sensor (Yan et al., 2023; Liang et al., 2024; Liu et al., 2023a; Zheng et al., 2023b).

Most multi-modal sensor fusion methods can be categorized into two methods. The first is deeply coupled fusion (DCF), which directly combines feature maps (FMs) extracted by sensor-specific encoder, as illustrated in Fig. 1-(a). While it is simple to implement and computationally efficient with excellent performance in various benchmarks (Chae et al., 2024; Liu et al., 2023a; Liang et al., 2024; Zhao et al., 2024a; Caesar et al., 2020; Geiger et al., 2013), it assumes all sensors are functioning properly and consistently. This makes DCF vulnerable to sensor degradation due to adverse weathers, surface-damages, and sensor failure. Moreover, DCF requires retraining the entire neural network when the number of sensors changes, as the size of the fused FM (i.e., the input to the detection

*corresponding author

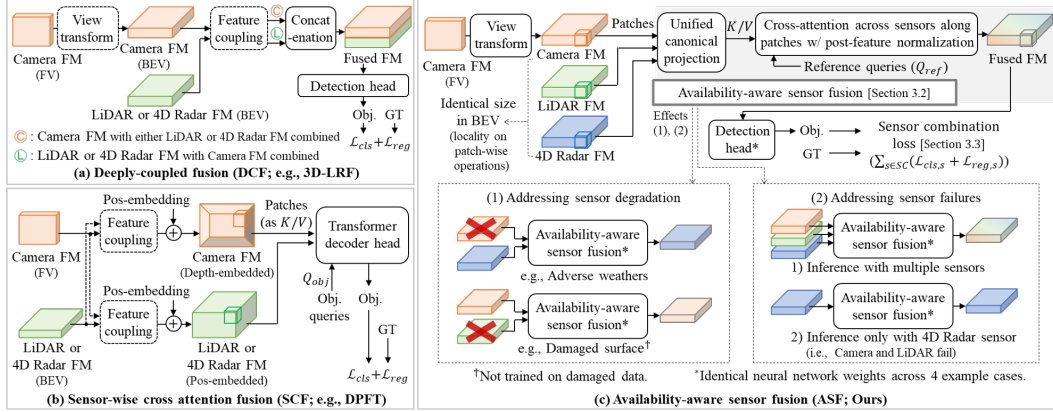


Figure 1: Comparison of sensor fusion methods: (a) DCF (e.g., 3D-LRF (Chae et al., 2024)), (b) SCF (e.g., CMT (Yan et al., 2023)), and (c) ASF. FV, BEV, Obj., GT, \mathcal{L}_{cls} and \mathcal{L}_{reg} stand for ‘front-view’, ‘bird’s eye-view’, ‘objects’, ‘ground truths’, ‘classification loss’, and ‘regression loss’, respectively. ‘Feature coupling’ refers to methods that combine features from multiple sensors to create new features. Optional components are in dashed lines; for example, (Vora et al., 2020) combines camera and LiDAR features without transforming the camera viewpoint, while (Yan et al., 2023) fuses features through a transformer decoder head (Carion et al., 2020) without explicit feature coupling. ASF does not apply feature coupling to ensure independence between sensors.

head) changes. The second method is sensor-wise cross-attention fusion (SCF), which divides features extracted from each sensor into patches with positional-embedding (e.g., depth information for camera (Liu et al., 2022; Wang et al., 2022)) and selectively combines available patches using cross-attention (Fig. 1-(b)), allowing it to handle cases where some sensors are degraded. However, SCF does not have sensor scalability, since the method does not project sensor-specific features into a standardized representation (Zheng et al., 2024; Liu et al., 2023b; Wang et al., 2016). In addition, SCF incurs computational complexity that scales with the number of patches, resulting in substantial computational overhead when processing multiple sensors with numerous patches (Fent et al., 2024; Yan et al., 2023; Bai et al., 2022).

One of the fundamental limitations of existing fusion methods stems from inconsistencies in feature representation across different sensors (Shashua, 2024; Yeong et al., 2025). Cameras produce 2D RGB images, whereas LiDAR generates 3D point clouds, and 4D Radar produces low-resolution tensors with power values. Therefore, each sensor extracts features with different representations for the same object, making consistent fusion challenging (as shown in Fig. 2-(a)). To address this inconsistency, an ideal strategy could project features from different sensors into a unified canonical space for fusion. The concept of ‘True Redundancy (Shashua, 2024)’, that ensures sensor independence while maintaining canonical feature representation for any sensor combination, suggests a promising direction for highly reliable and robust sensor fusion.

Therefore, we propose availability-aware sensor fusion (ASF) method (Fig. 1-(c)), in which each sensor performs independently while being complementarily fused through a projection to a unified canonical space. As a result, the proposed method addresses the limitations of both DCF and SCF simultaneously. The key innovation of ASF is in two sub-modules; First, unified canonical projection (UCP) projects features from each sensor into a unified space based on common criteria (i.e., canonical). Since UCP is optimized using the same reference query for all sensors, inconsistencies in sensor features are eliminated. While Fig. 2-(a) shows sensor features represented without clear patterns, Fig. 2-(b) demonstrates how UCP aligns the features from each sensor to the fused feature. Second, cross-attention across sensors along patches (CASAP) estimates the availability of sensors through patch-wise cross-attention on features projected into the unified canonical space, assigning higher weights to features from available sensors and lower weights to features from missing or degraded sensors. Unlike SCF that applies the cross-attention across all sensors (N_s) and patches (N_p) (i.e., $O(N_q N_s N_p)$ for N_q queries), ASF only applies the cross-attention across sensors along patches (i.e., $O(N_q N_s)$). Because of this, ASF eliminates complex positional-embedding and improves computationally efficiency. Additionally, it applies normalization to ensure that (camera, LiDAR,

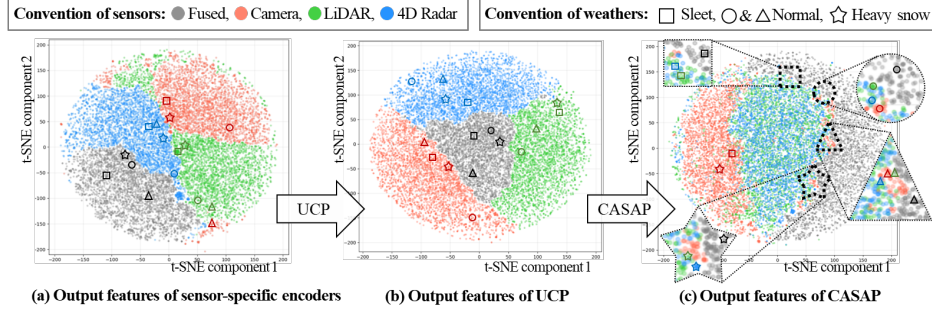


Figure 2: Visualization of feature representation with t-SNE (van der Maaten and Hinton, 2008) at different stages of ASF for ‘Sedan’ class. Red, green, blue, and gray dots represent features from camera, LiDAR, 4D Radar, and fused features, respectively. Symbols in solid lines such as circle and triangle, square, and star indicate normal, sleet, and heavy snow conditions, respectively. (a) Initial output features from sensor-specific encoders show inconsistent distribution across sensors. (b) After unified canonical projection (UCP), features become better aligned to the fused feature. (c) After cross-attention across sensors along patches (CASAP), features from available sensors form cohesive clusters (in dashed symbols) based on weather conditions. Note that in adverse weather, camera features show larger deviation due to the degradation. Additional visualizations are in Appendix B.

and 4D Radar) features can be processed consistently by the detection head regardless of sensor combination. In contrast to Fig. 2-(b), where each sensor’s features remain separate, Fig. 2-(c) shows how sensor features cluster together after CASAP (except for camera become useless in adverse weathers, as shown in Fig. 3). This enables ASF to flexibly handle sensor degradation or failure and to achieve the reliability embodied in the ‘True Redundancy’ concept (Shashua, 2024) for autonomous driving implementation.

To integrate the availability awareness into the detection head, we propose a sensor combination loss (SCL) that optimizes learning outcomes across all sensor combinations. SCL considers individual sensor unavailability during the training, enabling the system to maintain high performance in the presence of unexpected sensor failure or adverse weather conditions. The effectiveness of our proposed ASF method has been validated on the K-Radar dataset (Paek et al., 2022), demonstrating improvements of 9.7% in AP_{BEV} (87.2%) and 20.1% in AP_{3D} (73.6%) for detection performance at IoU=0.5 compared to state-of-the-art (SOTA) methods (Chae et al., 2024; Huang et al., 2025), which includes the performance in extreme situations such as sensor degradation or failure (i.e., unavailable).

The main contributions of this paper are as follows: (1) We propose ASF based on UCP and CASAP that achieves superior performance to SOTA methods and robust performance against sensor degradation and failure. (2) We propose SCL for the loss function to optimize the detection performance for all possible sensor combinations. (3) Through extensive experiments on the K-Radar dataset, we demonstrate that ASF achieves the high performance with low computational load.

The remainder of this paper is organized as follows: Section 2 introduces existing methods, and Section 3 describes the proposed ASF in detail. Section 4 presents experimental settings and results on the K-Radar dataset, analyzing performance in various scenarios including sensor degradation and failure. Section 5 concludes the paper with a summary and discusses the limitations. All codes and logs for ASF are available at <https://github.com/kaist-avelab/k-radar>.

2 Related Works

2.1 Deeply Coupled Fusion (DCF)

DCF constructs a fused feature map (FM) by concatenating FMs from each sensor. Most studies focus on fusing camera with LiDAR or 4D Radar (Liu et al., 2023a; Liang et al., 2024; Zheng et al., 2023b; Xiong et al., 2023), or combining LiDAR and 4D Radar (Chae et al., 2024; Huang et al., 2025). Implementations range from directly fusing the front-view (FV) camera image with LiDAR or 4D Radar without view transformation (Vora et al., 2020) to applying learnable BEV transforms

(Phillion and Fidler, 2020) and concatenating at the BEV stage (Liu et al., 2023a; Liang et al., 2024; Zheng et al., 2023b). DCF method is straightforward to implement and computationally efficient compared to SCF, demonstrating strong performance across multiple benchmarks.

Recent DCF studies have improved performance by applying feature coupling, where the FMs of each sensor are enhanced with FMs of other sensors using multi-layer perception (MLP) or attention mechanisms (Vaswani et al., 2017). 3D-LRF (Chae et al., 2024) demonstrated superior performance to the conventional DCFs (Liang et al., 2024; Liu et al., 2023a) by applying attention between LiDAR and 4D Radar voxel features before concatenation. L4DR (Huang et al., 2025) achieved SOTA performance on the K-Radar dataset by weighting each sensor’s FM using coupled BEV FMs with LiDAR and 4D Radar. However, DCF assumes all sensors are functioning normally, as they rely on the fused FM constructed by concatenating FMs from all sensors, making DCF vulnerable to sensor degradation and failure. This limitation arises because the training process does not expose the model to potential sensor degradation or failure scenarios that commonly occur during deployment.

2.2 Sensor-wise Cross-attention Fusion (SCF)

SCF divides sensor-specific FMs into patches and dynamically combines them through cross-attention in a transformer decoder head (Yan et al., 2023), inherently accommodating sensor availability. TransFusion (Bai et al., 2022) is the first SCF that addresses sensor availability, but its sequential fusion method (e.g., performing LiDAR detection first and then fusing with camera data) makes inference impossible when LiDAR is unavailable. CMT (Yan et al., 2023) presents an availability-aware sensor fusion of camera and LiDAR data using a transformer decoder head without applying feature coupling to individual sensors. However, without feature coupling for camera, CMT relies on positional embedding to incorporate depth information into camera FMs (Liu et al., 2022), which results in 3D patches ($H \times W \times D$). This leads to computational complexity of $O(N_q N_s N_p)$ (where N_q , N_s , and N_p are the number of queries, sensors, and patches, respectively), causing explosive growth in computational cost and memory usage. For instance, CMT requires 8 A100 GPUs with 80GB VRAM to train with a batch size of 16.

Recently, DPFT (Fent et al., 2024) creates independent FMs and projects sensor-agnostic query points onto different FMs to verify sensor availability, achieving 56.1% AP_{3D} at IoU=0.3 (using only 4D Radar and camera). Unlike methods that utilize entire FMs, DPFT achieves reasonable computational efficiency by employing deformable attention (Xia et al., 2022) that considers varying receptive fields using only a small number of key points. However, similar to CMT, DPFT performs object detection using variable object queries, which does not establish a common representation across different sensors (as illustrated in Fig. 2).

3 Proposed Methods

3.1 Sensor Fusion Framework

The overall sensor fusion framework consists of three stages: (1) sensor-specific encoders (i.e., backbones) that extract same-sized bird’s eye-view (BEV) feature maps (FMs) from each sensor data (i.e., RGB image, LiDAR point cloud, and 4D Radar tensor), (2) the proposed availability-aware sensor fusion (ASF) network that is described in following subsection 3.2, and (3) a detection head that detects objects from the fused FM.

Focusing on our ASF contribution, we utilize established methods for the sensor-specific encoders and detection head. Specifically, we adopt BEVDepth (Li et al., 2023), SECOND (Yan et al., 2018), and RTNH (Paek et al., 2022) backbones for camera, LiDAR, and 4D Radar, respectively, along with a SSD detection head (Liu et al., 2016). Further specifications regarding the overall sensor fusion framework, such as sensor-specific encoders and detection head, are provided in Appendix A.

3.2 Availability-aware Sensor Fusion (ASF)

As illustrated in Fig. 1-(c), the proposed ASF consists of two key components: unified canonical projection (UCP) and cross-attention across sensors along patches (CASAP).

Unified Canonical Projection (UCP). One of the key challenge in multi-modal sensor fusion is the inherent inconsistency of features from different sensors (Shashua, 2024; Yeong et al., 2025), as

visualized in Fig. 2-(a). To tackle this, we divide BEV FMs into an equal number of patches for all sensors and train projection functions to transform features from each sensor into a unified space based on the same criteria (i.e., reference query in CASAP). To formally define our methods, we first represent the same-sized FMs of each sensor as:

$$\mathbf{FM}^s \in \mathbb{R}^{C_s \times H \times W}, s \in \{S_C, S_L, S_R\}, \quad (1)$$

where C_s denotes the channel dimension for sensor s , H and W represent the identical height and width of BEV FMs for all sensors, respectively, and S_C , S_L , and S_R denote camera, LiDAR, and 4D Radar sensors, respectively. Each FM is then divided into patches \mathbf{F}_p^s with height P_H and width P_W :

$$\mathcal{T}_p(\mathbf{FM}^s) = \{\mathbf{F}_{p,i}^s | \mathbf{F}_{p,i}^s \in \mathbb{R}^{C_s \times P_H \times P_W}, i = 1 : N_p\}, \quad (2)$$

where $\mathcal{T}_p(\cdot)$ is the operation that divides each FM into patches, $N_p = (H/P_H) \times (W/P_W)$ is the number of patches, which is identical across all sensors since each FM has the same spatial size, and ‘ $1 : N_p$ ’ denotes ‘ $1, 2, \dots, N_p$ ’. Note that since the patches are already spatially aligned (i.e., $\mathbf{F}_{p,i}^{S_C}$, $\mathbf{F}_{p,i}^{S_L}$, and $\mathbf{F}_{p,i}^{S_R}$ correspond to the same position), our method eliminates the use of computationally expensive positional-embedding (Liu et al., 2022) required for SCF (Yan et al., 2023; Fent et al., 2024). Then, we apply a parallel operation along patches that projects each patch to have the same channel dimension C_u . This is the UCP operation $\mathcal{U}^s(\cdot)$ that transforms sensor-specific patches into patches in a unified canonical space. The UCP-processed patch \mathcal{P}_u^s for each sensor is expressed as:

$$\mathcal{P}_u^s = \{\mathbf{F}_{u,i}^s | \mathbf{F}_{u,i}^s = \mathcal{U}^s(\text{LN}(\mathbf{F}_{p,i}^s)) \in \mathbb{R}^{C_u}, i = 1 : N_p\} \quad (3)$$

$$\mathcal{U}^s(\cdot) = \text{LN}(\text{Proj}^{(n_u)}(\cdot)), \text{Proj}(\cdot) = \text{GeLU}(\text{MLP}(\cdot)), \quad (4)$$

where LN and n_u denote layer normalization (Ba et al., 2016) for training stability and the number of sequential projection functions incorporating MLP for transformation and GeLU (Hendrycks and Gimpel, 2016) for non-linearity, respectively. While our framework allows for repetition of the projection function to increase non-linearity, with 1 or 2 repetitions being sufficient (we use $n_u = 2$, which aligns features as demonstrated in Fig. 2-(b)). Note that \mathcal{U}^s is trained separately for each sensor based on reference query, which results in alignment of features from all sensors with respect to the fused feature as shown in Fig. 2-(b).

Cross-attention Across Sensors Along Patches (CASAP). The patches \mathbf{F}_u^s projected into the unified canonical space by UCP serve as keys (K) and values (V) for a trainable reference query $\mathbf{Q}_{ref} \in \mathbb{R}^{N_q \times C_u}$ (where N_q is the number of queries Q), and we perform cross-attention across sensors along patches as:

$$\mathbf{Q}'_{ref,i} = \text{CrossAttn}(Q = \mathbf{Q}_{ref}, K \& V \in \{\mathbf{F}_{u,i}^{S_C}, \mathbf{F}_{u,i}^{S_L}, \mathbf{F}_{u,i}^{S_R}\}), i = 1 : N_p, \quad (5)$$

where $\mathbf{Q}'_{ref,i}$ is the output of the cross-attention applied across sensors for the i -th patch. Since \mathbf{Q}_{ref} is trained primarily on features that are mostly available in the training data, it naturally develops high correlation (i.e., high attention scores) with patches from available sensors after the training. Consequently, during inference, $\mathbf{Q}'_{ref,i}$ is predominantly composed of available \mathbf{F}_u^s . The number of heads in cross-attention is a hyper-parameter whose impact is analyzed in subsection 4.4.

Compared to ASF, cross-attention in SCF is performed across all patches with respect to object queries \mathbf{Q}_{obj} in the transformer decoder head. This can be mathematically expressed as:

$$\mathbf{Q}'_{obj} = \text{CrossAttn}^{(n_{td})}(Q = \mathbf{Q}_{obj}, K \& V \in \{\mathbf{F}_{pe,1}^{S_C}, \dots, \mathbf{F}_{pe,N_p}^{S_C}, \mathbf{F}_{pe,1}^{S_L}, \dots, \mathbf{F}_{pe,N_p}^{S_L}, \mathbf{F}_{pe,1}^{S_R}, \dots, \mathbf{F}_{pe,N_p}^{S_R}\}), \quad (6)$$

where \mathbf{F}_{pe}^s represents patches with positional-embedding, and n_{td} (usually larger than 6 (Liu et al., 2022; Yan et al., 2023)) is the number of stacked transformer decoders. Eq. 6 shows the cross-attention across all sensors and all patches (i.e., the $K \& V$ set contains $N_s N_p$ patches, resulting in $O(N_q N_s N_p)$ computational complexity for N_q queries). In contrast, in Eq. 5, the cross-attention is applied across sensors and along patches, which requires only $O(N_q N_s)$ computational operations. This is a significant computational costs reduction as $N_s \ll N_p$. Moreover, as demonstrated in Fig. 3 and Tab. 1, ASF achieves better performance with only a single cross-attention layer than SCF utilizing stacked cross-attention layers (i.e., $n_{td} \geq 6$).

Sequentially, ASF applies post-feature normalization (PN) \mathcal{N} that has a similar structure to $\mathcal{U}^s(\cdot)$ with LN, to ensure that features can be processed consistently by the detection head regardless of

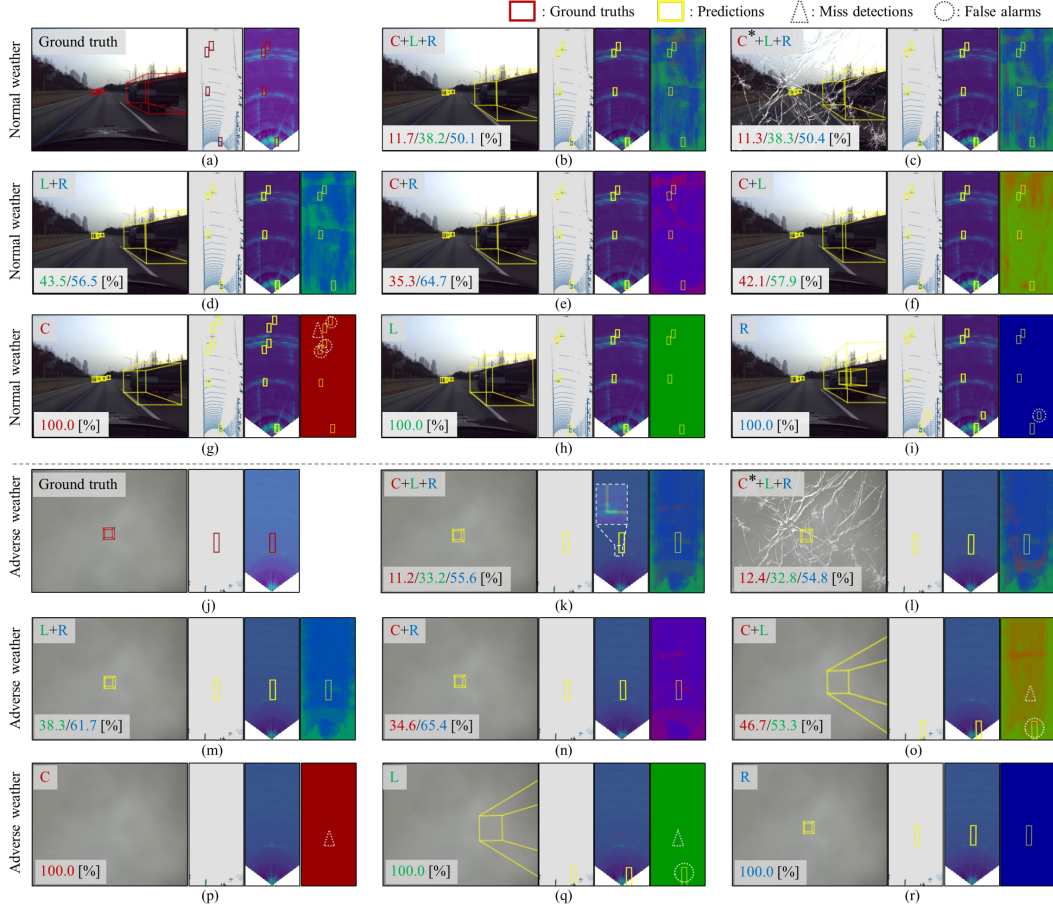


Figure 3: Qualitative results of ASF for various sensor combinations. We show results for normal and adverse weather conditions in (a-i) and (j-r), respectively, where employed sensors are noted in the top-left corner (C: Camera, L: LiDAR, R: 4D Radar, C*: damaged camera). Each subplot visualizes front-view camera image, LiDAR point cloud, 4D Radar tensor, and a sensor attention map (SAM) showing attention score distribution from cross-attention in CASAP. In the SAMs, red, green, and blue represent attention scores for Camera, LiDAR, and 4D Radar, respectively. For example, a predominantly blue SAM indicates that 4D Radar receives the highest attention scores, meaning that 4D Radar is used primarily for detection in the scene. The bottom-left corner of each subplot shows the proportion of attention scores in colored percentages (C/L/R[%]). Note that predictions are visualized on all sensor data, even when a sensor is not employed for detection (e.g., predictions from L+R are also visualized on the camera image).

the sensor combination. Therefore, PN enables camera, LiDAR, and 4D Radar features for the same object to be consistent. The set of patches \mathcal{P}_n with PN is formulated as:

$$\mathcal{P}_n = \{\mathbf{F}_{n,i} | \mathbf{F}_{n,i} = \mathcal{N}(\text{LN}(\mathbf{Q}'_{ref,i})) \in \mathbb{R}^{C_u}, i = 1 : N_p\} \quad (7)$$

$$\mathcal{N}(\cdot) = \text{LN}(\text{Proj}^{(n_n)}(\cdot)), \text{Proj}(\cdot) = \text{GeLU}(\text{MLP}(\cdot)), \quad (8)$$

where n_n denotes the number of sequential projections, with 1 or 2 being sufficient to increase non-linearity. Unlike Fig. 2-(b) where features from different sensors occupy distinct regions, Fig. 2-(c) illustrates how PN causes sensor features to converge into unified clusters.

Finally, to transform \mathcal{P}_n back to the original BEV size ($H \times W$), we apply a reshape operation $\mathcal{T}_n(\cdot)$. Since the size of \mathcal{P}_n is $C_u \times N_p = C_u \times N_H \times N_W = C_u \times (H/P_H) \times (W/P_W)$, the fused FM $\mathbf{FM}_{\text{fused}}$ can be obtained as:

$$\mathbf{FM}_{\text{fused}} = \mathcal{T}_n(\mathcal{P}_n \in \mathbb{R}^{C_u \times N_p}) \in \mathbb{R}^{C_q \times H \times W}, \quad (9)$$

Table 1: Performance comparison of 3D object detection on K-Radar (Paek et al., 2022) benchmark v1.0. C, L, and R represent Camera, LiDAR, and 4D Radar, respectively. The **bold** and underlined values indicate the best and the second-best, respectively. Note that the two ASF models for sensors L+R and C+L+R share the same neural network weights trained with C+L+R, which means that ASF for L+R represents a scenario where camera becomes unavailable. Nor., Ove., Sle., L.s., and H.s. denote ‘Normal’, ‘Overcast’, ‘Sleet’, ‘Light snow’, and ‘Heavy snow’, respectively.

Methods	Sensors	IoU	Metric	Total	Nor.	Ove.	Fog	Rain	Sle.	L.s.	H.s.
RTNH (Paek et al.)	R	0.3	BEV	41.1	41.0	44.6	45.4	32.9	50.6	81.5	56.3
			3D	37.4	37.6	42.0	41.2	29.2	49.1	63.9	43.1
		0.5	BEV	36.0	35.8	41.9	44.8	30.2	34.5	63.9	55.1
			3D	14.1	19.7	20.5	15.9	13.0	13.5	21.0	6.36
RTNH (Paek et al.)	L	0.3	BEV	76.5	76.5	88.2	86.3	77.3	55.3	81.1	59.5
			3D	72.7	73.1	76.5	84.8	64.5	53.4	80.3	52.9
		0.5	BEV	66.3	65.4	87.4	83.8	73.7	48.8	78.5	48.1
			3D	37.8	39.8	46.3	59.8	28.2	31.4	50.7	24.6
3D-LRF (Chae et al.)	L+R	0.3	BEV	84.0	83.7	89.2	95.4	78.3	60.7	88.9	74.9
			3D	74.8	81.2	87.2	86.1	73.8	49.5	87.9	67.2
		0.5	BEV	73.6	72.3	88.4	86.6	76.6	47.5	79.6	64.1
			3D	45.2	45.3	55.8	51.8	38.3	23.4	60.2	36.9
L4DR (Huang et al.)	L+R	0.3	BEV	79.5	86.0	89.6	89.9	81.1	62.3	89.1	61.3
			3D	78.0	77.7	80.0	88.6	79.2	60.1	78.9	51.9
		0.5	BEV	77.5	76.8	88.6	89.7	78.2	59.3	80.9	53.8
			3D	53.5	53.0	64.1	73.2	53.8	46.2	52.4	37.0
ASF (Proposed)	L+R	0.3	BEV	88.6	88.1	90.3	99.0	89.1	80.4	89.4	78.7
			3D	87.3	86.6	89.8	90.7	88.6	<u>80.0</u>	88.8	77.5
		0.5	BEV	87.0	86.2	90.2	90.8	88.8	<u>78.2</u>	88.6	71.0
			3D	72.9	64.6	86.6	79.6	73.4	70.0	77.6	66.7
	C+L+R	0.3	BEV	88.6	88.2	90.2	98.9	89.0	80.4	89.2	78.4
			3D	87.4	87.0	90.1	90.7	88.2	80.0	88.6	77.4
		0.5	BEV	87.2	86.7	90.1	90.8	88.7	78.3	88.3	70.9
			3D	73.6	71.8	87.0	79.4	73.0	67.5	78.0	66.4

where C_q is the quotient of $C_u/(P_H \times P_W)$ as we design $C_u = P_H \times P_W \times C_q$. Since the resulting channel dimension C_q may be insufficient for containing feature representation due to reduced channel dimensions after reshaping, in the implementation, we increase the number of patches by a factor of n_p (i.e., $N_p = N_H \times N_W \rightarrow N_p = n_p \times N_H \times N_W$). Consequently, the channel dimension of $\mathbf{FM}_{\text{fused}}$ increases from C_q to $n_p \times C_q$, and impact of this modification is evaluated in subsection 4.4.

3.3 Sensor Combination Loss (SCL)

Leveraging the consistent size of $\mathbf{FM}_{\text{fused}}$ (which serves as the input to the detection head) regardless of sensor combinations, we propose an SCL that enables simultaneous optimization across multiple sensor configurations. The proposed SCL is formalized as:

$$\mathcal{L}_{SCL} = \sum_{s \in SC} (\mathcal{L}_{cls,s} + \mathcal{L}_{reg,s}), \quad (10)$$

where SC represents the set of 7 possible sensor combinations (S_C -only, S_L -only, S_R -only, $S_L + S_R$, $S_C + S_R$, $S_C + S_L$, and $S_C + S_L + S_R$), where S_C , S_L , and S_R denote camera, LiDAR, and 4D Radar, respectively. $\mathcal{L}_{cls,s}$ and $\mathcal{L}_{reg,s}$ are the classification and regression losses for each sensor combination. SCL explicitly prepares for the potential sensor unavailability by optimizing across all sensor combinations in the training, enabling the model to recognize that available sensors perform better than others (e.g., 4D Radar outperform camera in adverse weather). As demonstrated in Tab. 4, SCL enhances the performance of the proposed ASF method when compared to ASF without SCL.

Table 2: Comparison of VRAM and FPS evaluated on the K-Radar benchmark v1.0. The **bold** and underlined values indicate the best and the second-best, respectively. The unit of VRAM and FPS are GB and Hz, respectively.

Methods	Sensors	VRAM	FPS
3D-LRF (Chae et al.)	L+R	1.2	5.04
DPFT (Fent et al.)	C+R	4.0	11.5
ASF (Proposed)	L+R	<u>1.5</u>	20.5
	C+L+R	1.6	<u>13.5</u>

4 Experiments

4.1 Experimental Setup

Dataset and Metrics. K-Radar (Paek et al., 2022) is a large-scale autonomous driving dataset with a broad range of conditions including time (day, night), weather (normal, rain, fog, snow, sleet), road types (urban, highway, mountain), and sensors (4D Radar, LiDAR, camera, GPS). Notably, K-Radar is the only dataset with data captured in adverse weather conditions.

For comparison with SOTA methods, we utilize two K-Radar benchmark variants. Benchmark v1.0 (Paek et al., 2022; Chae et al., 2024; Huang et al., 2025) focuses on the ‘Sedan’ class within a driving corridor region of $[0\text{m}, 72\text{m}] \times [-6.4\text{m}, 6.4\text{m}] \times [-2\text{m}, 6\text{m}]$ (X×Y×Z). For ablation studies and qualitative analysis, we use benchmark v2.0, which covers a wider area $[0\text{m}, 72\text{m}] \times [-16\text{m}, 16\text{m}] \times [-2\text{m}, 7.6\text{m}]$ and includes both ‘Sedan’ and ‘Bus or Truck’ classes. We evaluate using AP_{3D} and AP_{BEV} at IoU thresholds of 0.3 and 0.5, while also reporting VRAM usage and FPS based on the same hardware setup.

Implementation Details. We implement the ASF on a single RTX3090 GPU with 24GB VRAM. ASF is trained for 11 epochs using AdamW (Loshchilov and Hutter, 2017) optimizer with a learning rate 0.001 and a batch size 2. The voxel size for the fused FM is set to 0.4m, consistent with (Paek et al., 2022).

4.2 Comparison of ASF to SOTA Methods

Following the benchmark v1.0 of the K-Radar (Paek et al., 2022), we compare the proposed ASF with SOTA methods including 3D-LRF (Chae et al., 2024) and L4DR (Huang et al., 2025), and we use RTNH (Paek et al., 2022) for single-sensor performance. In addition to the detection performance comparison with DCF methods (Chae et al., 2024; Huang et al., 2025), we evaluate computational efficiency against DPFT (Fent et al., 2024) which is the only open-sourced SCF method available for K-Radar.

Detection Performance. As shown in Tab. 1, ASF significantly outperforms SOTA methods across various weather conditions. Compared to previous SOTA L4DR (Huang et al., 2025), ASF achieves substantial improvements of 9.7% in AP_{BEV} (87.2% vs. 77.5%) and 20.1% in AP_{3D} (73.6% vs. 53.5%) at IoU=0.5. These improvements are particularly remarkable in challenging conditions like sleet (67.5% vs. 46.2% AP_{3D}) and heavy snow (66.4% vs. 37.0% AP_{3D}). Notably, both ASF configurations (L+R and C+L+R) use identical neural network

weights yet maintain comparable performance, demonstrating the system’s ability to gracefully handle sensor degradation. Even with only LiDAR and Radar, ASF achieves 87.0% AP_{BEV} and 72.9% AP_{3D} at IoU=0.5, nearly matching the full sensor suite’s performance.

Table 3: Performance comparison of ASF under various sensor combinations on K-Radar (Paek et al., 2022) benchmark v2.0. We indicate the employed sensors (C: Camera, L: LiDAR, R: 4D Radar) and report AP_{3D} at IoU = 0.3 for ‘Sedan’ and ‘Bus or Truck’ classes. ‘Nor.’, ‘Ove.’, ‘Sle.’ and ‘H.s.’ refer to ‘Normal’, ‘Overcast’, ‘Sleet’, and ‘Heavy snow’, respectively. * denotes the sensor unavailability, as shown in Fig. 3. The **bold** and underlined values indicate the best and the second-best, respectively. All ten ASF models share the same neural network weights trained for R+L+C. Performance under additional weather conditions (Fog, Rain, and Light Snow) and with other evaluation metric AP_{BEV} is provided in Appendix D.

Class	Sensors	Total	Nor.	Ove.	Sle.	H.s.
Sedan	R	47.3	40.7	58.8	45.9	56.5
	L	73.0	73.0	86.1	64.9	54.5
	C	14.8	14.9	7.71	-	-
	C*	3.71	3.72	3.17	-	-
	L+R	77.3	77.7	87.3	74.4	65.4
	C+R	52.7	49.1	62.4	46.0	57.2
	C+L	76.4	<u>78.3</u>	86.5	64.2	57.1
	C+L+R	79.3	78.8	87.6	<u>74.2</u>	65.8
	C*+L+R	<u>77.6</u>	78.2	87.7	74.4	<u>65.4</u>
C+L*+R	58.9	58.8	66.6	52.3	58.2	
Bus or Truck	R	34.2	22.9	40.9	21.1	51.2
	L	54.9	53.7	74.8	69.1	37.8
	C	9.59	9.02	17.2	-	-
	C*	3.65	3.66	0.00	-	-
	L+R	59.9	52.5	71.6	68.2	68.9
	C+R	36.2	24.4	41.4	23.4	56.5
	C+L	53.0	49.1	60.1	72.1	39.6
	C+L+R	60.4	<u>52.7</u>	77.4	69.2	<u>68.9</u>
	C*+L+R	60.1	52.1	<u>72.0</u>	<u>70.9</u>	69.1
C+L*+R	40.0	31.5	38.2	28.9	54.8	

Computational Efficiency. ASF achieves exceptional computational efficiency for real-time autonomous driving applications. As demonstrated in Tab. 2, ASF with LiDAR and 4D Radar processes at 20.5 Hz, approximately 4× faster than 3D-LRF (5.04 Hz) using identical sensors. Even with all three sensors, ASF maintains 13.5 Hz, exceeding the 10 Hz threshold typically required for autonomous driving systems (Zhao et al., 2024b). This efficiency results from our CASAP, which applies cross-attention across sensors along patches rather than across all sensors and patches. Furthermore, ASF maintains a compact memory footprint (1.5-1.6 GB), comparable to 3D-LRF (1.2 GB) and substantially lower than DPFT (4.0 GB).

4.3 Addressing Sensor Degradation and Failure

A key advantage of ASF is the robust performance under sensor degradation or failure. As shown in Tab. 3 and Fig. 3, ASF dynamically adapts to different sensor combinations without retraining. Under normal conditions (Fig. 3-(a-i)), ASF effectively utilizes all available sensors with attention weights distributed according to each sensor’s reliability. However, ASF’s true value emerges in challenging scenarios. In adverse weather (Fig. 3-(j-r)), camera and LiDAR measurements are significantly degraded or disappear completely. In these critical situations, ASF automatically redistributes attention toward the more reliable 4D Radar, as evidenced by the predominant blue coloration in the sensor attention maps (SAMs) and corresponding attention percentages. Even with damaged sensors (denoted by * in Tab. 3 and Fig. 3), ASF maintains near-optimal performance. For example, with a damaged camera (C*), C*+L+R shows 77.6% AP_{3D} , which is only 1.7% lower than with fully sensors (79.3%). This robustness stems from the unified canonical projection (which creates a common feature space) and the cross-attention mechanism (which estimates sensor reliability).

The qualitative results in Fig. 3 demonstrate that in adverse weather, when LiDAR measurements disappear and camera visibility severely degrades, reliable object detection is only possible with active 4D Radar and ASF is fully using 4D Radar. Note that all results shown are from the same ASF model with identical weights, illustrating how ASF dynamically adjusts attention to maintain detection performance across varying sensor availabilities.

4.4 Ablation Studies

Tab. 4 presents ablation studies of key ASF components, analyzing five factors: patch size (P), channel dimension (C_u), patches multiplier (n_p), number of attention heads (n_h), and sensor combination loss (SCL). Our findings reveal that smaller patch sizes ($P=2$) improve performance through finer feature extraction, while balancing reduced channel dimension ($C_u=256$) with increased patches multiplier ($n_p=8$) maintains or enhances results; furthermore, increasing attention heads ($n_h = 16$) benefits ‘Bus or Truck’ detection, and incorporating SCL consistently improves performance across configurations by enhancing robustness to varying sensor availability. The optimal configuration combines $P=2$, $C_u=256$, $n_p=8$, $n_h=16$ with SCL.

Table 4: Ablation study of ASF. ASF performance for different components and parameters: P (patch size), C_u (channel dimension in unified canonical space), n_p (number of patches multiplier), n_h (number of heads in CASAP) and SCL, using AP_{3D} at IoU=0.3 for both ‘Sedan’ and ‘Bus or Truck’ on the K-Radar benchmark v2.0.

Exp.	P	C_u	n_p	n_h	SCL	Sedan	Bus
(a)	5	512	1	8		76.1	45.7
(b)	5	512	4	8		76.4	47.4
(c)	2	512	4	8		77.2	49.7
(d)	2	256	8	8		77.6	57.9
(e)	2	256	8	8	✓	79.3	58.2
(f)	2	256	8	16		77.5	60.2
(g)	2	256	8	16	✓	79.3	60.4

5 Conclusion

This paper introduces availability-aware sensor fusion (ASF), which addresses sensor availability challenges in autonomous driving by transforming features into a unified canonical space through UCP and CASAP. Our approach maintains computational efficiency ($O(N_q N_s)$) while providing robust fusion for sensor degradation or failure. The proposed sensor combination loss further enhances robustness by optimizing across all possible sensor combinations. Experiments on the K-Radar dataset demonstrate significant improvements over SOTA methods (9.7% in AP_{BEV} and

20.1% in AP_{3D} at $\text{IoU}=0.5$), with consistent performance across various weather conditions and sensor combinations.

Limitations. Despite ASF’s strong performance, the camera network’s capabilities remain a limitation. As shown in Fig. 3-(g) and (p), camera-based object detection is less precise, particularly in adverse weather. In Fig. 2-(c), while LiDAR and 4D Radar features are well integrated, camera features remain more separated in feature space. Enhancing the camera backbone could further boost system performance, especially in favorable weather conditions, where visual information is valuable.

Appendix

The appendix is organized as follows. Section A provides detailed explanations of the sensor fusion framework, including specific implementations of sensor-specific encoders and the detection head. Section B presents additional t-SNE visualizations that demonstrate the effectiveness of the unified canonical space. Section C analyzes attention score distributions across different weather conditions and distance ranges. Section D includes comprehensive performance results across various sensor combinations and alternative stereo camera configurations.

A Details of Sensor Fusion Framework

As shown in Fig. 4, the sensor fusion framework is divided into three stages: (1) sensor-specific encoders (Liu et al., 2021; Phillion and Fidler, 2020; Yan et al., 2018; Shi et al., 2020; Paek et al., 2022; Kong et al., 2024) that extract feature maps (FMs) from different types of multi-modal sensors (e.g., camera, LiDAR, and 4D Radar), (2) a fusion method that integrates these FMs, and (3) a task-dependent detection head. Stage

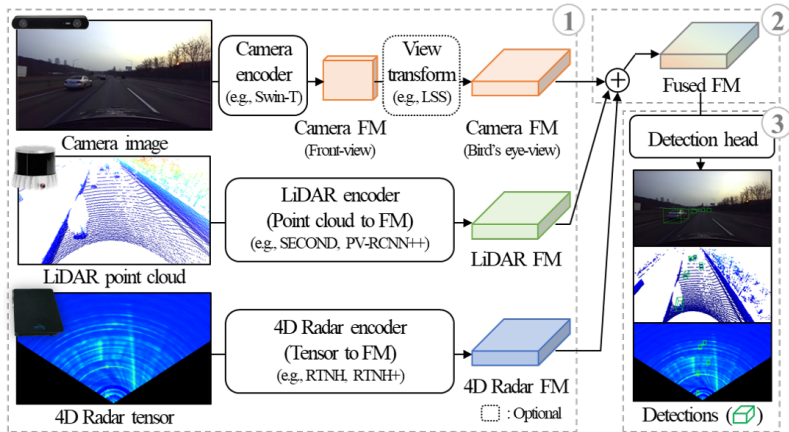


Figure 4: Overall sensor fusion framework for camera, LiDAR, and 4D Radar. ‘FM’ denotes ‘feature map’.

(1) has evolved independently for each sensor (Dosovitskiy et al., 2021; Lang et al., 2019; Paek et al., 2022), while stage (3) employs a task-dependent method (e.g., YOLO head (Redmon et al., 2016) for object detection) regardless of sensor type. Therefore, in this work, we propose a fusion method focusing on stage (2) rather than stages (1) and (3). Details of both existing and proposed fusion methods are illustrated in Fig. 1. In this section, we describe both the sensor-specific encoders and the detection head of the proposed availability-aware sensor fusion (ASF).

A.1 Sensor-specific Encoders

Sensor-specific encoders extract FMs from data of each sensor. Because different sensors provide data in different modalities—cameras produce 2D RGB images, LiDAR generates 3D point clouds, and 4D Radar outputs low-resolution tensors with power values—research on these encoders has evolved independently for each sensor type.

For ASF, we adopt established backbone architectures for each sensor and pre-train these backbones before ASF training. Each encoder is trained for 11 epochs following the K-Radar (Paek et al., 2022) training protocol. During ASF training, we freeze all sensor-specific encoders to ensure that only the ASF components and detection head are learned. Specifically, ‘UCP’ and ‘CASAP’ are

the ASF components updated during ASF training, which denote *unified canonical projection* and *cross-attention across sensors along patches*, respectively. Details for each encoder are as follows:

Camera. Camera-based sensor encoders for autonomous driving typically require transforming front-view (FV) images into a bird’s-eye-view (BEV) format for 3D object detection. Current approaches can be broadly categorized into two methods: (1) learnable BEV transformations such as Lift-Splat-Shoot (LSS) (Phillion and Fidler, 2020; Liu et al., 2023a; Liang et al., 2024), or (2) maintaining FV while using transformer decoders (Liu et al., 2022) that incorporate depth information as positional embeddings in BEV space. Although methods like PETR (Liu et al., 2022) have improved 3D object detection by injecting depth embeddings, they inevitably increase computational complexity due to the additional depth dimension. These two approaches form the foundation of camera-based fusion (Xiong et al., 2023; Zheng et al., 2023b; Liu et al., 2023a; Liang et al., 2024; Yan et al., 2023), commonly seen in deeply coupled fusion (DCF) and sensor-wise cross-attention fusion (SCF).

To develop a computationally efficient method, we opt for the LSS approach and adopt BEVDepth (Li et al., 2023), which supervises the LSS depth estimation using LiDAR point clouds. For encoding images, we use the Swin-S model of SwinTransformer as the 2D backbone, achieving 83% top-1 accuracy on ImageNet (Russakovsky et al., 2015). We resize front camera images to 704×256 pixels for encoding. The encoded 2D FMs are projected into BEV FMs via LSS with a grid size of 0.2 m. To match the 0.4 m grid size used in K-Radar, we add a convolutional layer with stride 2. During training, we employ the depth information projected from LiDAR point clouds onto the image and, inspired by (Yang et al., 2023), we use the LiDAR backbone’s (SECOND) BEV FMs for distillation. As shown in Fig. 3, camera images have limited utility in adverse weather, so we train the camera encoder only on normal or overcast scenes (sequences 1–20) from K-Radar.

A limitation of this approach is that promising stereo or multi-view detection models cannot be fully leveraged, because the K-Radar dataset (Paek et al., 2022)—the only one offering camera, LiDAR, and 4D Radar data in adverse weather—provides object annotations only for the front view. Moreover, unlike the KITTI dataset with its longer stereo baseline of 0.54 m, K-Radar uses waterproof ZED cameras with a baseline of just 0.12 m, limiting stereo-based detection for distant objects. Consequently, we employ a monocular camera method despite inherent performance constraints.

LiDAR. LiDAR provides precise depth information in the form of dense point clouds, often used as a reference for labeling other sensors (Paek et al., 2022; Sun et al., 2024). We adopt the SECOND (Yan et al., 2018) model as the LiDAR encoder, which is open-source in K-Radar and widely used in various benchmarks. Leveraging LiDAR’s high spatial resolution, we set the voxel size to 0.05 m and apply multiple layers of sparse convolution to generate BEV FMs with a 0.4 m grid size.

4D Radar. Unlike LiDAR, which uses Time-of-Flight (ToF) measurement, Radar detects spatial information through signal processing, which can introduce sidelobe noise. Traditional 3D Radar typically filters out noisy measurements to produce a sparse point cloud focusing on object presence (Paek and Guan, 2024). In contrast, 4D Radar captures additional elevation information, yielding higher-density point clouds (Zhang et al., 2023). This property is exemplified by K-Radar (Paek et al., 2022, 2023). We adopt RTNH (Paek et al., 2022), the baseline provided in K-Radar, as our 4D Radar encoder, following the original network settings and design.

A.2 Detection Head

Following the K-Radar baseline, we use an SSD detection head (Liu et al., 2016; Simon et al., 2018) for the 3D object detection task. Our implementation uses two anchor boxes per object class, oriented at 0° and 90° . Each anchor box is parametrized by eight values: the 3D center coordinates (x_c, y_c, z_c) , 3D size (x_l, y_l, z_l) , and orientation $(\cos(\text{yaw}), \sin(\text{yaw}))$, as in (Simon et al., 2018).

To address the severe class imbalance in object detection (negative samples far outnumber positives), we use the focal loss (Lin et al., 2017) for classification. For bounding box regression, we use smooth L1 loss to measure differences between predictions and ground truth, improving training stability. During inference, we select the class with the highest logit score for each proposal, then apply non-maximum suppression to remove redundant overlapping detections, producing the final predictions.

B t-SNE Visualizations

B.1 Additional t-SNE Visualizations

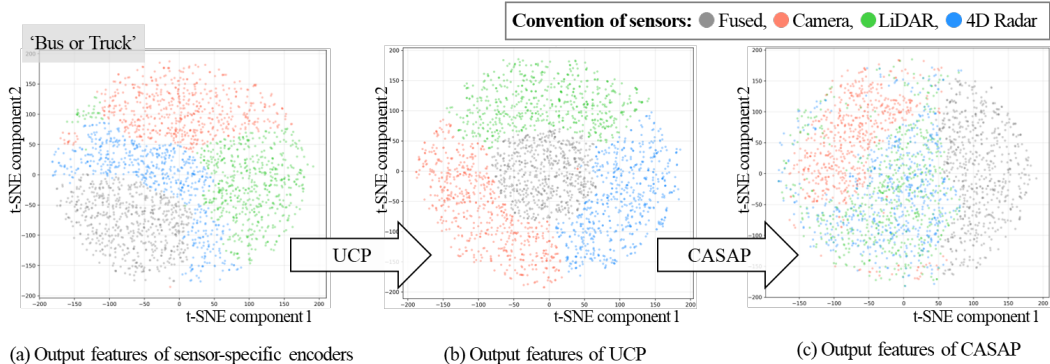


Figure 5: Visualization of feature representations through t-SNE (van der Maaten and Hinton, 2008) at different stages of the proposed ASF for the ‘Bus or Truck’ class. ‘UCP’ and ‘CASAP’ denote *unified canonical projection* and *cross-attention across sensors along patches*, which are the two main components of the proposed ASF.

This section provides additional feature visualizations to complement those in Fig. 2, which only shows results for the ‘Sedan’ class. Fig. 5 presents t-SNE (van der Maaten and Hinton, 2008) visualizations of the ‘Bus or Truck’ class at different stages of the ASF. These visualizations further demonstrate how ASF unifies feature representations from different sensors.

Consistent with Fig. 2, we observe three main trends in the t-SNE visualizations. First, the initial features from the sensor-specific encoders are scattered without clear alignment across different sensors. Next, after UCP, sensor-specific features become better aligned with the fused features. Finally, following CASAP, features from available sensors form cohesive clusters (in this case, LiDAR and 4D Radar).

These findings underscore the effectiveness of ASF in creating a unified canonical space for multi-sensor features. Note that in K-Radar, the ‘Sedan’ class has 37,213 instances, whereas the ‘Bus or Truck’ class has 7,449 instances, leading to sparser data in Fig. 5 compared to Fig. 2.

B.2 Details of t-SNE Visualizations

To visualize object-specific features in each sensor’s feature map (FM), we use RoIAlign (He et al., 2017) to crop features within bounding boxes. RoIAlign extracts fixed-size FMs, making it suitable for t-SNE (which requires consistent dimensions). We then visualize these cropped features in the unified canonical space. For those extracted before projection (where channel dimensions may differ), we downsample as needed to ensure consistent feature dimensions.

C Analysis of Attention Scores across Sensors

Table 5: Attention scores ratios [%] across different weather conditions

Sensor	Normal	Overcast	Fog	Rain	Sleet	Light Snow	Heavy Snow
Camera	11.6	11.1	11.3	11.1	11.1	10.9	11.0
LiDAR	39.5	37.5	37.5	37.3	35.9	36.3	34.7
4D Radar	48.9	51.4	51.2	51.6	53.0	52.8	54.3

Tables 5 and 6 show the attention score ratios for each sensor according to weather conditions and distance from the ego-vehicle. Intuitively, a higher attention score ratio indicates greater utilization of the corresponding sensor in ASF. Note that the sensor attention maps (SAMs) in Fig. 3 visualize the attention scores for each sensor.

Table 6: Attention scores ratios [%] across different distance ranges

Sensor	0-8m	8-16m	16-24m	24-32m	32-40m	40-48m	48-56m	56-64m	64-72m
Camera	9.8	10.1	10.4	10.9	11.1	11.3	11.9	12.7	13.4
LiDAR	48.4	40.2	37.2	36.0	34.9	34.8	35.0	35.5	36.0
4D Radar	41.8	49.7	52.4	53.1	54.0	53.9	53.1	51.8	50.6

As shown in Tab. 5, the attention score ratios of camera and LiDAR decrease under severe adverse weather conditions such as sleet and heavy snow (camera: 11.6% to 11.0%, LiDAR: 39.5% to 34.7%), while 4D Radar shows the opposite trend, increasing from 48.9% to 54.3%. This demonstrates that 4D Radar is more robust than camera and LiDAR in adverse weather conditions and provides available measurements when other sensors degrade.

Furthermore, as shown in Tab. 6, LiDAR’s attention score ratio decreases as distance increases (from 48.4% at 0-8m to 36.0% at 64-72m), while camera’s attention score increases (from 9.8% to 13.4%). This indicates that ASF relies more on camera measurements at longer ranges where LiDAR becomes sparse. In contrast, 4D Radar maintains a relatively consistent attention ratio (41.8% to 50.6%) regardless of distance. Notably, 4D Radar shows the highest absolute attention scores compared to camera and LiDAR across most conditions. While camera lacks depth information and LiDAR provides very sparse measurements in 3D space, 4D Radar leverages dense tensor data, which enables more reliable feature extraction for sensor fusion.

D Additional Detection Results

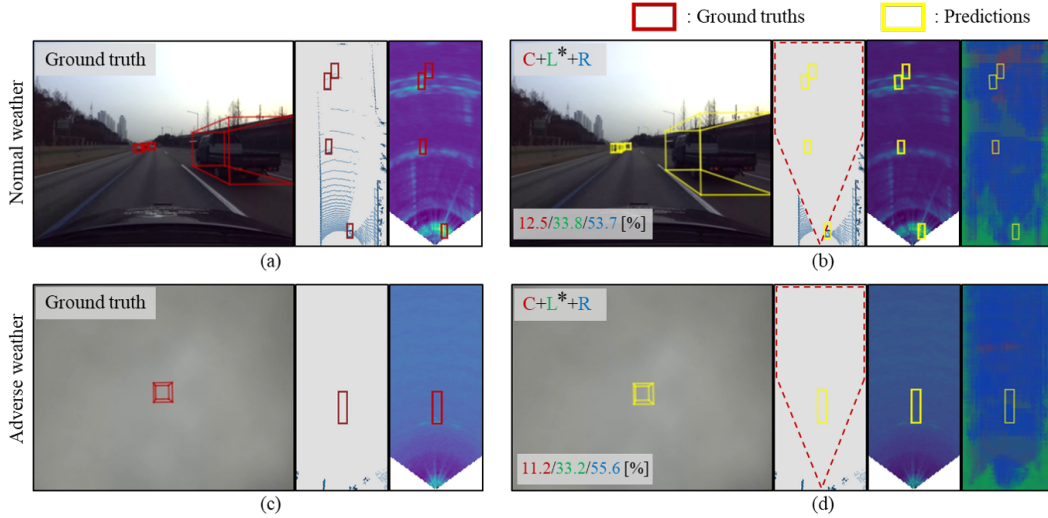


Figure 6: Qualitative results of ASF with C+L*+R (C: Camera, L*: damaged LiDAR, R: 4D Radar). We show results under (a–b) normal and (c–d) adverse weather conditions. Each grid shows the camera image, LiDAR point cloud, 4D Radar tensor, and a sensor attention map (SAM) illustrating attention scores from CASAP (except for (a) and (c), which only show sensor data for ground truth visualization). In the SAM, red, green, and blue represent attention to camera, LiDAR, and 4D Radar, respectively. For example, a predominantly blue SAM indicates that 4D Radar has the highest attention in that scene. The bottom-left corner of each grid shows attention score proportions (C/L/R [%]). Yellow and red boxes denote predictions and ground truth, respectively.

This section presents additional detection results for ASF. First, we provide qualitative results demonstrating ASF’s robustness when the LiDAR sensor is damaged, shown in the same road environment as Fig. 3, along with additional results from diverse road scenarios. Second, we demonstrate the robustness of ASF (C+L+R) with respect to random seeds by presenting experimental results on the K-Radar (Paek et al., 2022) benchmark v1.0 using 10 different random seeds (0 to 8 and 2025), complementing Tab. 1 which reports results only for seed 2025. Third, we evaluate alternative

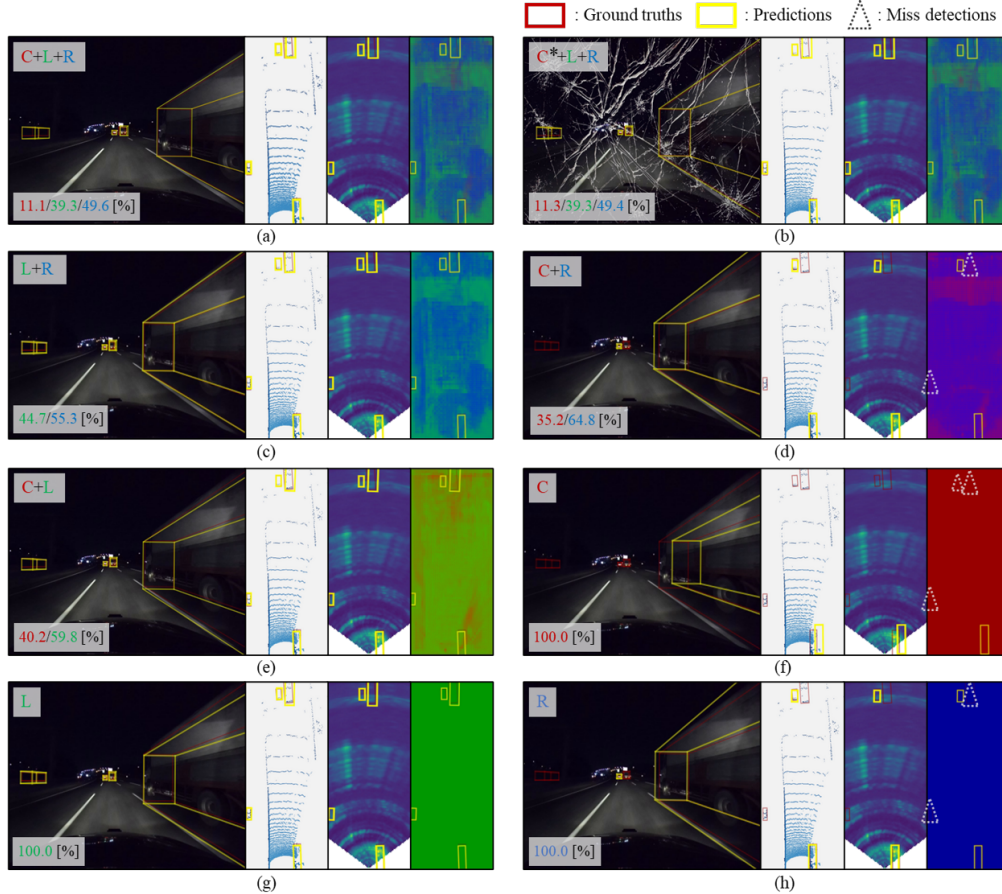


Figure 7: Qualitative results of ASF for various sensor combinations. We show results low-light nighttime roads. Each grid shows the camera image, LiDAR point cloud, 4D Radar tensor, and a SAM illustrating attention scores from CASAP. In the SAM, red, green, and blue represent attention to camera, LiDAR, and 4D Radar, respectively. The bottom-left corner of each grid shows attention score proportions ($C/L/R$ [%]). Yellow and red boxes denote predictions and ground truth, respectively, which are displayed in all panels. Dotted triangles indicate miss detections and are marked in the SAM. Note that predictions are visualized on all sensor data, even when a sensor is not employed for detection (e.g., predictions from L+R are also visualized on the camera image).

camera backbone architectures, including stereo camera-based methods, to assess the impact of improved camera encoders on the overall fusion performance. Finally, we provide comprehensive quantitative performance on K-Radar benchmark v2.0, including AP_{3D} and AP_{BEV} for both ‘Sedan’ and ‘Bus or Truck’ classes at IoU=0.3 and 0.5, complementing Tab. 3 which reports only AP_{3D} at IoU=0.3.

D.1 Additional Qualitative Results

Damaged LiDAR. When LiDAR surfaces are damaged or contaminated, LiDAR measurements can be lost (Schlager et al., 2022). In adverse conditions such as heavy snow, accumulation on the LiDAR sensor can block forward measurements, as illustrated by the red dashed line in Fig. 6-(d), even though vehicles are present. We also simulate total loss of forward LiDAR returns from surface damage (e.g., broken sensor), as seen in Fig. 6-(b). Despite missing LiDAR data, ASF still detects all objects using only camera and 4D Radar inputs. As reported in Tab. 3, ASF with C+L*+R often performs similarly or even better than C+R alone. Compared to Fig. 3-(b), the sensor attention map (SAM) in Fig. 6-(b) confirms the increased reliance on camera or 4D Radar when LiDAR is unavailable.

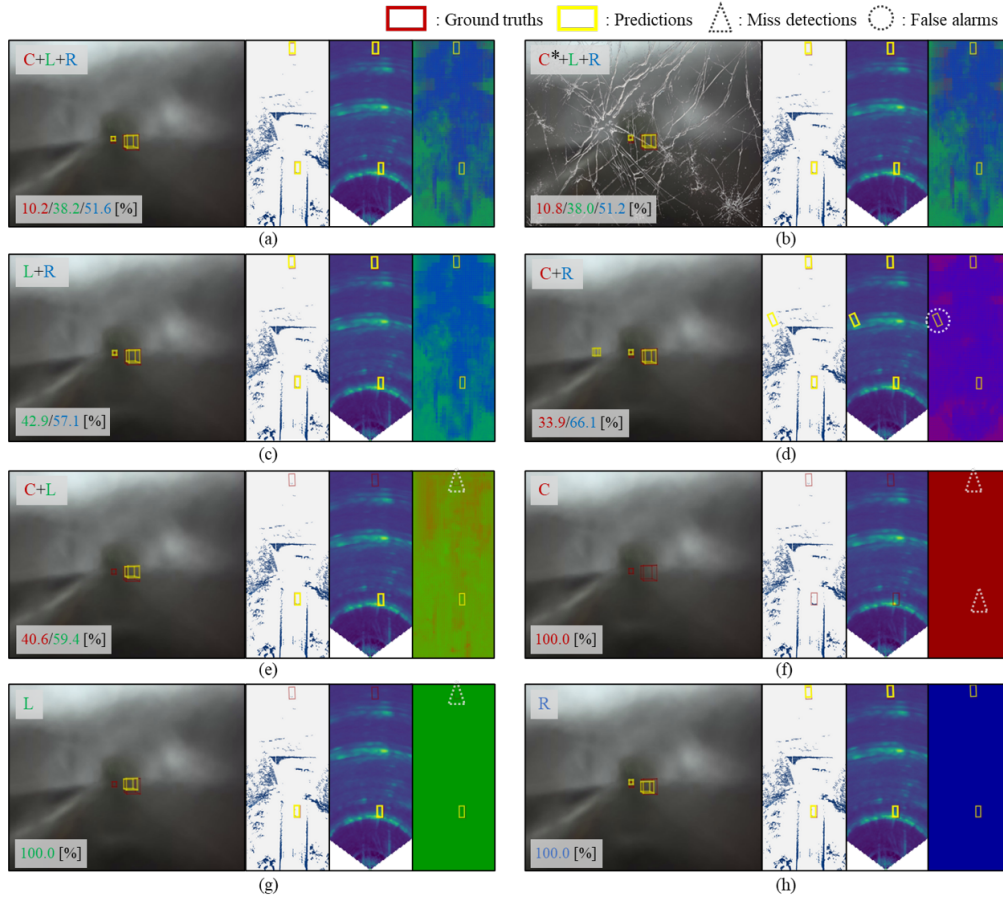


Figure 8: Qualitative results of ASF for various sensor combinations. We show results under adverse weather conditions. Each grid shows the camera image, LiDAR point cloud, 4D Radar tensor, and a SAM illustrating attention scores from CASAP. In the SAM, red, green, and blue represent attention to camera, LiDAR, and 4D Radar, respectively. The bottom-left corner of each grid shows attention score proportions (C/L/R [%]). Yellow and red boxes denote predictions and ground truth, respectively, which are displayed in all panels. Dotted triangles and circles indicate miss detections and false alarms, respectively, and are marked in the SAM. Note that predictions are visualized on all sensor data, even when a sensor is not employed for detection (e.g., predictions from L+R are also visualized on the camera image).

Additional Results Visualization. Fig. 7 shows the inference results for multiple vehicles in low-light road environments. When detection is performed using camera-only in low-illumination conditions, numerous miss detections occur, as shown in Fig. 7-(f). Additionally, as shown in Fig. 7-(h), in the case of 4D Radar, one of the distant vehicles aligned side by side is covered by the reflection of another vehicle, resulting in miss detection. Furthermore, the leftmost vehicle experiences miss detection as the radio waves are blocked by the road barrier. In the case of Fig. 7-(a), which utilizes all of 4D Radar, LiDAR, and camera, stable and accurate detection is possible without miss detections.

Fig. 8 shows the inference results for multiple vehicles in adverse weather conditions. As shown in Fig. 8-(e), when only LiDAR is utilized, nearby vehicles can be detected due to the presence of measurements, but distant vehicles experience miss detection due to the absence of measurements. In contrast, as shown in Fig. 8-(h), 4D Radar has measurements regardless of distance, enabling stable detection without miss detections. Similar to Fig. 7-(a), in the case of Fig. 8-(a), which utilizes all of 4D Radar, LiDAR, and camera, stable and accurate detection is possible without miss detections and false alarms.

D.2 Additional Quantitative Results

Table 7: Additional performance comparison of ASF (C+L+R) under various weather conditions on the K-Radar (Paek et al., 2022) benchmark v1.0. We report both AP_{BEV} and AP_{3D} at IoU = 0.3 for the ‘Sedan’ class, showing mean and standard deviation across 10 random seeds (0 to 8 and 2025).

Metric	Total	Normal	Overcast	Fog	Rain	Sleet	Light snow	Heavy snow
AP_{BEV}	88.64 ±0.12	88.24 ±0.12	90.29 ±0.09	98.97 ±0.27	88.93 ±0.17	86.24 ±2.85	89.25 ±0.11	78.44 ±0.16
AP_{3D}	87.48 ±0.21	86.96 ±0.17	89.94 ±0.20	90.67 ±0.08	88.28 ±0.20	80.46 ±0.21	88.92 ±0.22	76.03 ±2.33

Multiple Random Seeds. Tab. 7 presents the mean and standard deviation of ASF (C+L+R) performance across 10 random seeds on the K-Radar benchmark v1.0, demonstrating the robustness and generality of our approach. The low standard deviations (mostly below 0.3) indicate stable performance across different random initializations. Notably, the sleet and heavy snow condition shows higher variance (± 2.85 for AP_{BEV} and ± 2.33 for AP_{3D} , respectively), suggesting this weather condition presents more challenging and variable detection scenarios. The consistently high performance in Fog conditions ($98.97 AP_{BEV}$ and $90.67 AP_{3D}$) with minimal variance demonstrates ASF’s particular effectiveness in low-visibility scenarios where 4D Radar excels.

Table 8: Performance comparison of monocular and stereo camera-based networks on the K-Radar (Paek et al., 2022) benchmark v2.0. We report both AP_{BEV} and AP_{3D} at IoU = 0.3 for the ‘Sedan’ and ‘Bus or Truck’ classes. We note that camera performance is evaluated on sequences 1 to 20, which consist of normal weather conditions.

Metric	Class	BEVDepth (Mono)	DSGN++ (Stereo)	ASF (BEVDepth)	ASF (Stereo)
AP_{BEV}	Sedan	19.9	24.3	82.5	82.4
	Bus or Truck	13.4	24.8	70.2	67.2
AP_{3D}	Sedan	17.8	20.8	79.4	79.3
	Bus or Truck	11.5	22.5	60.4	59.5

Stereo Camera. As shown in Tab. 8, the stereo camera-based DSGN++ (Chen et al., 2022) achieves improved performance on K-Radar (24.8% and 22.5% AP_{3D} for Sedan and Bus or Truck, respectively) compared to the monocular camera-based BEVDepth (Li et al., 2023). We integrate DSGN++ as ASF’s camera-specific encoder. However, as shown in Tab. 8, ASF using DSGN++ shows comparable performance to ASF using BEVDepth. This may be attributed to two factors: (1) the detection performance of LiDAR and 4D Radar is significantly superior to that of the camera, and (2) K-Radar’s ZED 2i camera has a 12cm baseline compared to KITTI’s 54cm, limiting the improvement potential of stereo-based methods.

Performance on Benchmark v2.0. Tab. 9, 10, 11, and 12 present comprehensive evaluations of ASF performance across various sensor configurations and weather conditions on the K-Radar benchmark v2.0. Results demonstrate that multi-sensor fusion approaches consistently outperform single-sensor methods. The C+L+R configuration achieves the highest performance in most scenarios for both ‘Sedan’ and ‘Bus or Truck’ classes, with C*+L+R often ranking second, which indicates that a damaged camera does not significantly affect performance.

Performance analysis across weather conditions reveals that 4D Radar-inclusive combinations (C+L+R, L+R) exhibit superior performance in adverse weather (demonstrating 4D Radar’s effectiveness under challenging environmental conditions), particularly in fog and snow. While camera-LiDAR fusion (C+L) occasionally outperforms in normal and overcast conditions, its performance deteriorates significantly in precipitation.

Acknowledgment

This work was supported by the National Research Foundation of Korea (NRF) grant funded by the Korea government (MSIT) (No. 2021R1A2C3008370).

Table 9: Performance comparison of ASF under various sensor combinations evaluated on the K-Radar (Paek et al., 2022) benchmark v2.0. We indicate the employed sensors (C: Camera, L: LiDAR, R: 4D Radar) and report AP_{3D} at IoU = 0.3 under various weather conditions for the ‘Sedan’ and ‘Bus or Truck’ classes. The **bold** and underlined values indicate the best and the second-best, respectively. All ten ASF models share the same neural network weights trained with R+L+C.

Class	Sensors	Total	Normal	Overcast	Fog	Rain	Sleet	Light snow	Heavy snow
Sedan	R	47.3	40.7	58.8	84.4	41.0	45.9	66.1	56.5
	L	73.0	73.0	86.1	92.9	64.3	64.9	86.0	54.5
	C	14.8	14.9	7.7	-	-	-	-	-
	C*	3.7	3.7	3.2	-	-	-	-	-
	L+R	77.3	77.7	<u>87.3</u>	95.5	71.0	74.4	91.0	65.4
	C+R	52.7	49.1	62.4	84.6	44.6	46.0	66.5	57.2
	C+L	76.4	<u>78.3</u>	86.5	93.4	69.4	64.2	87.3	57.1
	C+L+R	79.3	78.8	86.1	93.7	72.9	<u>74.2</u>	91.2	65.8
	C*+L+R	<u>77.6</u>	78.2	87.7	<u>93.8</u>	<u>71.3</u>	74.4	<u>91.1</u>	<u>65.4</u>
	C+L*+R	58.9	59.2	64.0	92.4	47.7	65.4	66.5	58.2
Bus or Truck	R	34.2	22.9	41.0	-	0.2	21.1	83.5	51.2
	L	54.9	53.7	<u>74.8</u>	-	5.1	69.1	85.2	37.8
	C	9.6	9.0	17.2	-	-	-	-	-
	C*	3.7	3.7	0.0	-	-	-	-	-
	L+R	59.9	52.5	71.6	-	6.8	68.2	88.1	68.9
	C+R	36.2	24.4	41.4	-	0.3	23.4	82.1	56.5
	C+L	53.0	49.1	60.1	-	4.4	72.1	85.1	39.6
	C+L+R	60.4	<u>52.7</u>	77.4	-	8.0	69.2	<u>87.9</u>	68.9
	C*+L+R	<u>60.1</u>	52.1	72.0	-	8.4	<u>70.9</u>	<u>87.9</u>	69.1
	C+L*+R	40.0	31.5	38.2	-	0.4	28.9	81.0	54.8

References

- Claudine Badue, R nik Guidolini, Raphael Vivacqua Carneiro, Pedro Azevedo, Vinicius B Cardoso, Avelino Forechi, Luan Jesus, Rodrigo Berriel, Thiago M Paixao, Filipe Mutz, et al. Self-driving cars: A survey. *Expert systems with applications*, 165:113816, 2021.
- Zhangjing Wang, Yu Wu, and Qingqing Niu. Multi-sensor fusion in automated driving: A survey. *IEEE Access*, 8:2847–2868, 2020. doi: 10.1109/ACCESS.2019.2962554.
- Ziqiang Zheng, Yujie Cheng, Zhichao Xin, Zhibin Yu, and Bing Zheng. Robust perception under adverse conditions for autonomous driving based on data augmentation. *IEEE Transactions on Intelligent Transportation Systems*, 24(12):13916–13929, 2023a. doi: 10.1109/TITS.2023.3297318.
- Dong-Hee Paek, Seung-Hyun Kong, and Kevin Tirta Wijaya. K-radar: 4d radar object detection for autonomous driving in various weather conditions. *Advances in Neural Information Processing Systems*, 35:3819–3829, 2022.
- Andras Palffy, Ewoud Pool, Srimannarayana Baratam, Julian F. P. Kooij, and Darius M. Gavrilu. Multi-class road user detection with 3+1d radar in the view-of-delft dataset. *IEEE Robotics and Automation Letters*, 7(2):4961–4968, 2022. doi: 10.1109/LRA.2022.3147324.
- Seung-Hyun Kong, Dong-Hee Paek, and Sangyeong Lee. Rtnh+: Enhanced 4d radar object detection network using two-level preprocessing and vertical encoding. *IEEE Transactions on Intelligent Vehicles*, pages 1–14, 2024. doi: 10.1109/TIV.2024.3428696.
- Shunqiao Sun and Yimin D. Zhang. 4d automotive radar sensing for autonomous vehicles: A sparsity-oriented approach. *IEEE Journal of Selected Topics in Signal Processing*, 15(4):879–891, 2021. doi: 10.1109/JSTSP.2021.3079626.
- Junjie Yan, Yingfei Liu, Jianjian Sun, Fan Jia, Shuailin Li, Tiancai Wang, and Xiangyu Zhang. Cross modal transformer: Towards fast and robust 3d object detection. In *Proceedings of the IEEE/CVF International Conference on Computer Vision*, pages 18268–18278, 2023.

Table 10: Performance comparison of ASF under various sensor combinations evaluated on the K-Radar (Paek et al., 2022) benchmark v2.0. We indicate the employed sensors (C: Camera, L: LiDAR, R: 4D Radar) and report AP_{BEV} at IoU = 0.3 under various weather conditions for the ‘Sedan’ and ‘Bus or Truck’ classes. The **bold** and underlined values indicate the best and the second-best, respectively. All ten ASF models share the same neural network weights trained with R+L+C.

Class	Sensors	Total	Normal	Overcast	Fog	Rain	Sleet	Light snow	Heavy snow
Sedan	R	55.9	48.7	70.1	92.0	50.8	52.6	76.8	61.1
	L	76.7	78.1	93.8	93.6	70.0	67.8	88.4	58.2
	C	17.6	17.7	8.9	-	-	-	-	-
	C*	5.3	5.3	3.5	-	-	-	-	-
	L+R	81.8	80.7	94.3	98.1	75.7	81.0	93.6	69.6
	C+R	58.7	54.7	71.1	91.9	52.7	52.4	74.6	61.3
	C+L	79.3	81.0	94.9	95.1	72.5	68.3	89.7	59.5
	C+L+R	82.5	81.8	94.9	98.0	76.2	81.0	93.8	<u>69.5</u>
	C*+L+R	<u>82.1</u>	<u>81.1</u>	<u>94.7</u>	98.1	<u>76.0</u>	80.2	93.8	69.4
	C+L*+R	64.5	64.6	76.1	92.5	57.2	56.9	75.9	60.6
Bus or Truck	R	43.5	28.4	42.9	-	0.3	23.7	92.5	77.2
	L	63.1	57.0	75.5	-	6.2	72.3	88.7	61.3
	C	11.4	11.2	18.1	-	-	-	-	-
	C*	3.9	4.0	0.0	-	-	-	-	-
	L+R	69.5	58.3	75.2	-	7.3	71.3	<u>96.2</u>	89.7
	C+R	44.6	29.2	43.4	-	0.3	26.0	91.1	76.9
	C+L	61.8	53.1	68.0	-	5.3	75.5	90.0	64.7
	C+L+R	70.2	58.3	81.5	-	8.0	72.2	96.1	89.6
	C*+L+R	<u>70.0</u>	<u>58.2</u>	<u>75.7</u>	-	9.2	<u>73.8</u>	96.4	88.4
	C+L*+R	48.0	36.2	42.6	-	0.4	33.6	91.0	77.2

Tingting Liang, Hongwei Xie, Kaicheng Yu, Zhongyu Xia, Zhiwei Lin, Yongtao Wang, Tao Tang, Bing Wang, and Zhi Tang. Bevfusion: a simple and robust lidar-camera fusion framework. In *Proceedings of the 36th International Conference on Neural Information Processing Systems*, NIPS ’22, Red Hook, NY, USA, 2024. Curran Associates Inc. ISBN 9781713871088.

Zhijian Liu, Haotian Tang, Alexander Amini, Xinyu Yang, Huizi Mao, Daniela L Rus, and Song Han. Bevfusion: Multi-task multi-sensor fusion with unified bird’s-eye view representation. In *2023 IEEE international conference on robotics and automation (ICRA)*, pages 2774–2781. IEEE, 2023a.

Lianqing Zheng, Sen Li, Bin Tan, Long Yang, Sihan Chen, Libo Huang, Jie Bai, Xichan Zhu, and Zhixiong Ma. Rcfusion: Fusing 4-d radar and camera with bird’s-eye view features for 3-d object detection. *IEEE Transactions on Instrumentation and Measurement*, 72:1–14, 2023b. doi: 10.1109/TIM.2023.3280525.

Yujeong Chae, Hyeonseong Kim, and Kuk-Jin Yoon. Towards robust 3d object detection with lidar and 4d radar fusion in various weather conditions. In *2024 IEEE/CVF Conference on Computer Vision and Pattern Recognition (CVPR)*, pages 15162–15172, 2024. doi: 10.1109/CVPR52733.2024.01436.

Yun Zhao, Zhan Gong, Peiru Zheng, Hong Zhu, and Shaohua Wu. Simplebev: Improved lidar-camera fusion architecture for 3d object detection. *arXiv preprint arXiv:2411.05292*, 2024a.

Holger Caesar, Varun Bankiti, Alex H Lang, Sourabh Vora, Venice Erin Liong, Qiang Xu, Anush Krishnan, Yu Pan, Giancarlo Baldan, and Oscar Beijbom. nuscenes: A multimodal dataset for autonomous driving. In *Proceedings of the IEEE/CVF conference on computer vision and pattern recognition*, pages 11621–11631, 2020.

Andreas Geiger, Philip Lenz, Christoph Stiller, and Raquel Urtasun. Vision meets robotics: The kitti dataset. *The International Journal of Robotics Research*, 32(11):1231–1237, 2013.

Yingfei Liu, Tiancai Wang, Xiangyu Zhang, and Jian Sun. Petr: Position embedding transformation for multi-view 3d object detection. In *European Conference on Computer Vision*, pages 531–548. Springer, 2022.

Table 11: Performance comparison of ASF under various sensor combinations evaluated on the K-Radar (Paek et al., 2022) benchmark v2.0. We indicate the employed sensors (C: Camera, L: LiDAR, R: 4D Radar) and report AP_{3D} at IoU = 0.5 under various weather conditions for the ‘Sedan’ and ‘Bus or Truck’ classes. The **bold** and underlined values indicate the best and the second-best, respectively. All ten ASF models share the same neural network weights trained with R+L+C.

Class	Sensors	Total	Normal	Overcast	Fog	Rain	Sleet	Light snow	Heavy snow
Sedan	R	20.4	13.2	26.6	59.5	18.1	20.9	28.7	30.7
	L	41.1	38.5	43.1	67.8	37.1	34.1	52.4	35.4
	C	5.9	5.9	2.8	-	-	-	-	-
	C*	1.0	1.0	0.8	-	-	-	-	-
	L+R	52.1	49.0	56.9	<u>81.4</u>	48.2	45.1	59.6	50.1
	C+R	27.5	22.6	29.8	<u>66.2</u>	23.1	27.2	30.2	39.3
	C+L	<u>52.3</u>	52.3	50.0	79.4	45.7	40.1	65.9	42.7
	C+L+R	52.9	<u>50.5</u>	55.8	81.5	49.1	44.6	60.1	<u>50.0</u>
	C*+L+R	<u>52.3</u>	49.3	<u>56.8</u>	79.6	<u>48.9</u>	<u>45.0</u>	<u>60.3</u>	<u>50.0</u>
	C+L*+R	33.7	29.9	32.3	67.5	29.0	29.1	37.6	38.7
Bus or Truck	R	16.5	8.5	22.6	-	0.1	8.7	65.3	24.6
	L	29.1	22.1	38.0	-	1.1	44.2	66.2	20.5
	C	2.6	2.5	6.3	-	-	-	-	-
	C*	2.6	2.6	0.0	-	-	-	-	-
	L+R	<u>31.7</u>	<u>24.2</u>	52.6	-	2.8	44.4	<u>70.9</u>	<u>33.2</u>
	C+R	18.1	9.7	18.3	-	0.2	8.7	65.1	28.0
	C+L	31.2	22.5	33.6	-	0.9	51.4	69.6	21.2
	C+L+R	31.6	23.7	47.0	-	<u>2.5</u>	<u>45.0</u>	72.3	33.0
	C*+L+R	32.1	24.5	<u>48.2</u>	-	2.3	44.8	70.6	33.3
	C+L*+R	19.2	13.5	15.6	-	0.0	9.8	62.5	27.9

Yue Wang, Vitor Campagnolo Guizilini, Tianyuan Zhang, Yilun Wang, Hang Zhao, and Justin Solomon. Detr3d: 3d object detection from multi-view images via 3d-to-2d queries. In *Conference on Robot Learning*, pages 180–191. PMLR, 2022.

Xu Zheng, Yuanhuiyi Lyu, and Lin Wang. Learning modality-agnostic representation for semantic segmentation from any modalities. In *European Conference on Computer Vision*, pages 146–165. Springer, 2024.

Zhenghao Liu, Chenyan Xiong, Yuanhuiyi Lv, Zhiyuan Liu, and Ge Yu. Universal vision-language dense retrieval: Learning a unified representation space for multi-modal retrieval. In *International Conference on Learning Representations (ICLR)*, 2023b.

Liwei Wang, Yin Li, and Svetlana Lazebnik. Learning deep structure-preserving image-text embeddings. In *Proceedings of the IEEE conference on computer vision and pattern recognition*, pages 5005–5013, 2016.

Felix Fent, Andras Palffy, and Holger Caesar. DPFT: Dual perspective fusion transformer for camera-radar-based object detection. *IEEE Transactions on Intelligent Vehicles (T-IV)*, 2024.

Xuyang Bai, Zeyu Hu, Xinge Zhu, Qingqiu Huang, Yilun Chen, Hongbo Fu, and Chiew-Lan Tai. Transfusion: Robust lidar-camera fusion for 3d object detection with transformers. In *Proceedings of the IEEE/CVF conference on computer vision and pattern recognition*, pages 1090–1099, 2022.

Amnon Shashua. True Redundancy, 2024. URL <https://www.mobileye.com/technology/true-redundancy/>.

De Jong Yeong, Krishna Panduru, and Joseph Walsh. Exploring the unseen: A survey of multi-sensor fusion and the role of explainable ai (xai) in autonomous vehicles. *Sensors*, 25(3):856, 2025. doi: 10.3390/s25030856.

Sourabh Vora, Alex H Lang, Bassam Helou, and Oscar Beijbom. Pointpainting: Sequential fusion for 3d object detection. In *Proceedings of the IEEE/CVF conference on computer vision and pattern recognition*, pages 4604–4612, 2020.

Table 12: Performance comparison of ASF under various sensor combinations evaluated on the K-Radar (Paek et al., 2022) benchmark v2.0. We indicate the employed sensors (C: Camera, L: LiDAR, R: 4D Radar) and report AP_{BEV} at IoU = 0.5 under various weather conditions for the ‘Sedan’ and ‘Bus or Truck’ classes. The **bold** and underlined values indicate the best and the second-best, respectively. All ten ASF models share the same neural network weights trained with R+L+C.

Class	Sensors	Total	Normal	Overcast	Fog	Rain	Sleet	Light snow	Heavy snow
Sedan	R	40.8	30.0	54.7	85.6	36.9	39.6	65.2	48.4
	L	66.8	65.7	79.0	90.7	60.1	54.6	83.4	52.7
	C	8.8	8.9	4.3	-	-	-	-	-
	C*	2.1	2.1	1.1	-	-	-	-	-
	L+R	74.0	72.6	84.4	<u>96.1</u>	67.3	<u>67.4</u>	90.8	63.4
	C+R	45.8	39.7	57.2	<u>87.4</u>	40.7	41.6	66.7	53.9
	C+L	72.3	72.8	87.2	93.3	62.5	55.4	87.2	55.9
	C+L+R	74.5	74.8	<u>85.1</u>	96.2	<u>67.0</u>	67.5	90.8	63.5
	C*+L+R	<u>74.1</u>	<u>72.9</u>	85.0	<u>96.1</u>	<u>66.9</u>	66.7	90.7	63.2
	C+L*+R	53.1	54.5	57.0	61.5	50.2	50.3	68.5	55.2
Bus or Truck	R	23.8	14.2	30.0	-	0.2	12.7	87.3	64.3
	L	45.8	35.7	61.1	-	2.3	58.2	81.9	53.3
	C	11.4	11.2	18.1	-	-	-	-	-
	C*	2.7	2.8	0.0	-	-	-	-	-
	L+R	53.1	37.5	<u>59.8</u>	-	6.1	56.6	88.2	<u>80.1</u>
	C+R	31.9	14.4	25.9	-	0.2	13.4	90.1	64.7
	C+L	47.3	32.4	40.7	-	3.3	63.1	85.3	55.6
	C+L+R	53.9	<u>36.5</u>	54.7	-	<u>7.9</u>	59.3	90.4	80.4
	C*+L+R	<u>53.6</u>	36.1	57.5	-	8.0	<u>59.7</u>	90.8	<u>80.1</u>
	C+L*+R	33.2	20.9	24.7	-	0.2	18.3	88.0	61.4

Nicolas Carion, Francisco Massa, Gabriel Synnaeve, Nicolas Usunier, Alexander Kirillov, and Sergey Zagoruyko. End-to-end object detection with transformers. In *European conference on computer vision*, pages 213–229. Springer, 2020.

Laurens van der Maaten and Geoffrey Hinton. Visualizing data using t-sne. *Journal of Machine Learning Research*, 9:2579–2605, 2008.

Xun Huang, Ziyu Xu, Hai Wu, Jinlong Wang, Qiming Xia, Yan Xia, Jonathan Li, Kyle Gao, Chenglu Wen, and Cheng Wang. L4dr: Lidar-4dradar fusion for weather-robust 3d object detection. In *Proceedings of the 39th AAAI Conference on Artificial Intelligence (AAAI)*, 2025.

Weiyi Xiong, Jianan Liu, Tao Huang, Qing-Long Han, Yuxuan Xia, and Bing Zhu. Lxl: Lidar excluded lean 3d object detection with 4d imaging radar and camera fusion. *IEEE Transactions on Intelligent Vehicles*, 2023.

Jonah Philion and Sanja Fidler. Lift, splat, shoot: Encoding images from arbitrary camera rigs by implicitly unprojecting to 3d. In *Computer Vision—ECCV 2020: 16th European Conference, Glasgow, UK, August 23–28, 2020, Proceedings, Part XIV 16*, pages 194–210. Springer, 2020.

Ashish Vaswani, Noam Shazeer, Niki Parmar, Jakob Uszkoreit, Llion Jones, Aidan N Gomez, Łukasz Kaiser, and Illia Polosukhin. Attention is all you need. *Advances in neural information processing systems*, 30, 2017.

Zhuofan Xia, Xuran Pan, Shiji Song, Li Erran Li, and Gao Huang. Vision transformer with deformable attention. In *Proceedings of the IEEE/CVF conference on computer vision and pattern recognition*, pages 4794–4803, 2022.

Yinhao Li, Zheng Ge, Guanyi Yu, Jinrong Yang, Zengran Wang, Yukang Shi, Jianjian Sun, and Zeming Li. Bevdepth: Acquisition of reliable depth for multi-view 3d object detection. In *Proceedings of the AAAI conference on artificial intelligence*, volume 37, pages 1477–1485, 2023.

Yan Yan, Yuxing Mao, and Bo Li. Second: Sparsely embedded convolutional detection. In *Sensors*, volume 18, page 3337. MDPI, 2018.

- Wei Liu, Dragomir Anguelov, Dumitru Erhan, Christian Szegedy, Scott Reed, Cheng-Yang Fu, and Alexander C Berg. Ssd: Single shot multibox detector. In *Computer Vision–ECCV 2016: 14th European Conference, Amsterdam, The Netherlands, October 11–14, 2016, Proceedings, Part I 14*, pages 21–37. Springer, 2016.
- Jimmy Lei Ba, Jamie Ryan Kiros, and Geoffrey E Hinton. Layer normalization. *arXiv preprint arXiv:1607.06450*, 2016.
- Dan Hendrycks and Kevin Gimpel. Gaussian error linear units (gelus). *arXiv preprint arXiv:1606.08415*, 2016.
- Ilya Loshchilov and Frank Hutter. Decoupled weight decay regularization. *arXiv preprint arXiv:1711.05101*, 2017.
- Jingyuan Zhao, Wenyi Zhao, Bo Deng, Zhenghong Wang, Feng Zhang, Wenxiang Zheng, Wanke Cao, Jinrui Nan, Yubo Lian, and Andrew F. Burke. Autonomous driving system: A comprehensive survey. *Expert Systems with Applications*, 242:122836, 2024b. ISSN 0957-4174. doi: <https://doi.org/10.1016/j.eswa.2023.122836>.
- Ze Liu, Yutong Lin, Yue Cao, Han Hu, Yixuan Wei, Zheng Zhang, Stephen Lin, and Baining Guo. Swin transformer: Hierarchical vision transformer using shifted windows. In *Proceedings of the IEEE/CVF international conference on computer vision*, pages 10012–10022, 2021.
- Shaoshuai Shi, Chaoxu Guo, Li Jiang, Zhe Wang, Jianping Shi, Xiaogang Wang, and Hongsheng Li. Pv-rcnn: Point-voxel feature set abstraction for 3d object detection. In *Proceedings of the IEEE/CVF conference on computer vision and pattern recognition*, pages 10529–10538, 2020.
- Alexey Dosovitskiy, Lucas Beyer, Alexander Kolesnikov, Dirk Weissenborn, Xiaohua Zhai, Thomas Unterthiner, Mostafa Dehghani, Matthias Minderer, Georg Heigold, Sylvain Gelly, Jakob Uszkoreit, and Neil Houlsby. An image is worth 16x16 words: Transformers for image recognition at scale. In *International Conference on Learning Representations (ICLR)*, 2021. URL <https://openreview.net/forum?id=YicbFdNTTy>.
- Alex H Lang, Sourabh Vora, Holger Caesar, Lubing Zhou, Jiong Yang, and Oscar Beijbom. Pointpillars: Fast encoders for object detection from point clouds. In *Proceedings of the IEEE/CVF conference on computer vision and pattern recognition*, pages 12697–12705, 2019.
- Joseph Redmon, Santosh Divvala, Ross Girshick, and Ali Farhadi. You only look once: Unified, real-time object detection. In *Proceedings of the IEEE conference on computer vision and pattern recognition*, pages 779–788, 2016.
- Olga Russakovsky, Jia Deng, Hao Su, Jonathan Krause, Sanjeev Satheesh, Sean Ma, Zhiheng Huang, Andrej Karpathy, Aditya Khosla, Michael Bernstein, et al. Imagenet large scale visual recognition challenge. *International journal of computer vision*, 115:211–252, 2015.
- Yiran Yang, Dongshuo Yin, Xuee Rong, Xian Sun, Wenhui Diao, and Xinming Li. Beyond the limitation of monocular 3d detector via knowledge distillation. In *2023 IEEE/CVF International Conference on Computer Vision (ICCV)*, pages 9043–9052, 2023. doi: 10.1109/ICCV51070.2023.00833.
- Min-Hyeok Sun, Dong-Hee Paek, Seung-Hyun Song, and Seung-Hyun Kong. Efficient 4d radar data auto-labeling method using lidar-based object detection network. In *2024 IEEE Intelligent Vehicles Symposium (IV)*, pages 2616–2621, 2024. doi: 10.1109/IV55156.2024.10588669.
- Dong-Hee Paek and Junfeng Guan. Introduction to 4D radar: Hardware, MIMO, signal processing, dataset, and AI. Tutorial at 2024 IEEE Intelligent Vehicles Symposium, 6 2024. URL <https://www.ieee-iv-4dradar.org/>.
- Xinyu Zhang, Li Wang, Jian Chen, Cheng Fang, Lei Yang, Ziyang Song, Guangqi Yang, Yichen Wang, Xiaofei Zhang, and Jun Li. Dual radar: A multi-modal dataset with dual 4d radar for autonomous driving. *arXiv preprint arXiv:2310.07602*, 2023.

- Dong-Hee Paek, Seung-Hyun Kong, and Kevin Tirta Wijaya. Enhanced k-radar: Optimal density reduction to improve detection performance and accessibility of 4d radar tensor-based object detection. In *2023 IEEE Intelligent Vehicles Symposium (IV)*, pages 1–6. IEEE, 2023.
- Martin Simon, Stefan Milz, Karl Amende, and Horst-Michael Gross. Complex-yolo: An euler-region-proposal for real-time 3d object detection on point clouds. In *Proceedings of the European Conference on Computer Vision (ECCV) Workshops*, pages 197–209, 2018. doi: 10.1007/978-3-030-11009-3_11. URL <https://arxiv.org/abs/1803.06199>.
- Tsung-Yi Lin, Priya Goyal, Ross Girshick, Kaiming He, and Piotr Dollár. Focal loss for dense object detection. In *Proceedings of the IEEE international conference on computer vision*, pages 2980–2988, 2017.
- Kaiming He, Georgia Gkioxari, Piotr Dollár, and Ross Girshick. Mask r-cnn. In *Proceedings of the IEEE international conference on computer vision*, pages 2961–2969, 2017.
- Birgit Schlager, Thomas Goelles, Stefan Muckenhuber, and Daniel Watzenig. Contaminations on lidar sensor covers: Performance degradation including fault detection and modeling as potential applications. *IEEE Open Journal of Intelligent Transportation Systems*, 3:738–747, 2022. doi: 10.1109/OJITS.2022.3214094.
- Yilun Chen, Shijia Huang, Shu Liu, Bei Yu, and Jiaya Jia. Dsgn++: Exploiting visual-spatial relation for stereo-based 3d detectors. *IEEE Transactions on Pattern Analysis and Machine Intelligence*, 45(4):4416–4429, 2022.